Unveiling Challenging Microbial Fossil Biosignatures from Rio Tinto with Micro-to-Nanoscale Chemical and Ultrastructural Imaging

Lara Maldanis, David Fernandez-Remolar, Laurence Lemelle, Andrew H Knoll, Manuel Guizar-Sicairos, Mirko Holler, Francisco Mateus Cirilo da Silva, Valérie Magnin, Michel Mermoux, Alexandre Simionovici

Unveiling Challenging Microbial Fossil Biosignatures from Rio Tinto with Micro-to-Nanoscale Chemical and Ultrastructural Imaging

Lara Maldanis,[1,*] David Fernandez-Remolar,[2,3] Laurence Lemelle,[4] Andrew H. Knoll,[5] Manuel Guizar-Sicairos,[6,7] Mirko Holler,[6] Francisco Mateus Cirilo da Silva,[8,9] Valérie Magnin,[1] Michel Mermoux,[10] and Alexandre Simionovici[1,†]

Abstract

Understanding the nature and preservation of microbial traces in extreme environments is crucial for reconstructing Earth's early biosphere and for the search for life on other planets or moons. At Rio Tinto, southwestern Spain, ferric oxide and sulfate deposits similar to those discovered at Meridiani Planum, Mars, entomb a diversity of fossilized organisms, despite chemical conditions commonly thought to be challenging for life and fossil preservation. Investigating this unique fossil microbiota can elucidate ancient extremophile communities and the preservation of biosignatures in acidic environments on Earth and, potentially, Mars. In this study, we use an innovative multiscale approach that combines the state-of-the-art synchrotron X-ray nanoimaging methods of ptychographic X-ray computed laminography and nano-X-ray fluorescence to reveal Rio Tinto's microfossils at subcellular resolution. The unprecedented nanoscale views of several different specimens within their geological and geochemical contexts reveal novel intricacies of preserved microbial communities. Different morphotypes, ecological interactions, and possible taxonomic affinities were inferred based on qualitative and quantitative 3D ultrastructural information, whereas diagenetic processes and metabolic affinities were inferred from complementary chemical information. Our integrated nano-to-microscale analytical approach revealed previously invisible microbial and mineral interactions, which complemented and filled a gap of spatial resolution in conventional methods. Ultimately, this study contributes to the challenge of deciphering the faint chemical and morphological biosignatures that can indicate life's presence on the early Earth and on distant worlds. Key Words: Fossil Biosignatures—Microfossils—Geomicrobiology—Mars—Rio Tinto—Multiscale—X-Ray Nanoimaging—Ptychographic X-Ray Computed Laminography—Nano-X-Ray Fluorescence. Astrobiology 24, 721–733.

[1]ISTerre, Univ. Grenoble Alpes, Univ. Savoie Mont Blanc, CNRS, IRD, IFSTTAR, Grenoble, France.
[2]SKL Lunar and Planetary Sciences, Macau University of Science and Technology, Macau, China.
[3]CNSA Macau Center for Space Exploration and Science, Macau, China.
[4]LGL-TPE, ENS de Lyon, Univ. de Lyon, CNRS, Lyon, France.
[5]Department of Organismic and Evolutionary Biology, Harvard University, Cambridge Massachusetts, USA.
[6]Paul Scherrer Institute, Villigen PSI, Switzerland.
[7]Institute of Physics, École Polytechnique Fédérale de Lausanne (EPFL), Lausanne, Switzerland.
[8]Brazilian Synchrotron Light Laboratory, LNLS, Brazilian Center for Research in Energy and Materials, CNPEM, Campinas, Brazil.
[9]Institute of Physics, IFGW, Campinas University, UNICAMP, Campinas, Brazil.
[10]LEPMI, Univ. Grenoble Alpes, Univ. Savoie Mont Blanc, CNRS, Grenoble INP, 38000 Grenoble, France.
[†]Institut Universitaire de France (IUF).
*Current address: Earth Science Department, Vrije Universiteit Amsterdam, the Netherlands.

1. Introduction

The search for microbial life on Mars, whether past or present, is a primary driver of the Mars 2020 mission and planned Mars Sample Return missions (Farley and Williford, 2017). Environmental context for *in situ* and sample return missions has been established through geological mapping using orbiters and rovers, and rock cores have been collected for eventual detailed investigations in advanced laboratories on Earth (Simon et al., 2023). Compared to Earth, Mars' surface is dry, cold, and subject to high-radiation and oxidizing conditions, which limit prospects for extant life and can also destroy exposed organics. Nevertheless, the lack of plate tectonics has resulted in less intense metamorphism and lower diagenesis rates, which associated with the relatively slower weathering and erosion has allowed sedimentary rocks that date back to 4 Ga to remain preserved and accessible today (McMahon et al., 2018). At the time when life began to flourish on Earth, approximately 4–3.5 Ga (Allwood et al., 2007; Dodd et al., 2017; Nutman et al., 2016), Mars was undergoing the so-called Noachian–Hesperian transition ($\sim$3.7–3.5 Ga) from a planet with at least episodically abundant surface water, potentially capable of supporting microbial life, to the dry and hostile environments observable today (Sauterey et al., 2022). Terrestrial analogs of these terrains, such as Rio Tinto in southwestern Spain, provide important insights into the habitability and the potential for biosignature preservation in rocks similar in environmental settings to those of Mars. In this context, Rio Tinto provides a reference analog for Noachian–Hesperian transition deposits epitomized by the iron-rich acidic deposits on Meridiani Planum (Amils et al., 2007; Amils et al., 2014). Rio Tinto deposits show that, in combination, oxidation of sulfur species and seasonal evaporation can promote a concentration of iron oxides, as well as sulfate minerals, such as jarosite and schwertmannite, typically found at Meridiani (Fernández Remolar et al., 2005; Rapin et al., 2019).

In addition to providing a geochemical and mineralogical analog of iron-rich deposits on Mars, studies at Rio Tinto have revealed an unexpected past and present microbial diversity despite its extremely acidic conditions (mean pH 2.3) and high metal concentrations (Fe, Cu, Zn, As) (Fernández Remolar and Knoll, 2008; González-Toril et al., 2003; López-Archilla, Marin and Amils, 2001; Zettler et al., 2002) that are found locally. Partial preservation of biomolecules and body fossils in the iron-rich deposits of Rio Tinto challenges the perspective that rocks formed under iron rich, acidic, or oxidizing conditions are unsuitable for the preservation of organic material (Fenton, 1894; Sumner, 2004), which enhances astrobiological interest in the iron-rich terrains of Mars (McMahon et al., 2018). Reports on terrestrial analogs include the preservation of diverse lipids in acidic streams (Tan, Lewis and Sephton, 2018) and, in Rio Tinto terrains, peptide chains (Colín-García et al., 2011), large (>600 Da) fatty acids, hydrocarbons, isoprenoids, alkanols, hopanoids, and steroids (Fernández Remolar, et al., 2021b). Moreover, a diverse fossil assemblage has been reported from Rio Tinto sediments that includes insect cuticles, plant tissues, fungi, algae, and bacteria-like structures (Fernández Remolar and Knoll, 2008; Preston et al., 2011). The partial preservation of microbial fossils at up to 2.1 Ma in Rio Tinto terraces is ascribed to an early mineralization of the organisms by rapid precipitation of iron oxides from Fe-saturated solutions, generating molds and casts that persist through diagenesis (Fernández Remolar et al., 2005).

The study of fossil microorganisms found in 2.1 Ma iron-rich rocks of Rio Tinto highlights the analytical and interpretational challenges that will be encountered in the quest for traces of life in Fe-bearing rocks from Mars. The search for ancient traces of microbial life relies on an understanding of how microorganisms and the products of their activity can be preserved in rocks and how these evolve over geologic time scales. As in investigations of Precambrian fossils, details of morphology, ultrastructural features, taxonomic relationships, and ecological interactions need to be extracted from micrometer scale fossils in dense rock matrices (Des Marais et al., 2008; Javaux, 2019; Lepot, 2020). In Rio Tinto samples, the already difficult *in situ* colocalization of organics within fossilized microbial bodies is challenged by the lower preservation potential of biochemical compounds under acidic conditions and by the fact that fossils are embedded in iron oxide-bearing rocks. Assessment of the biogenicity, endogeneity, and syngenicity of microbial fossils also requires inspections of the morphological and geochemical features that span scales from macro to nano. This multiscale picture is necessary for combining subcellular information with inferences about a microbial, geological, and (paleo)environmental context (Lepot, 2020), all crucial for assessing putative traces of life in extreme environments and in ancient or heavily altered rocks (Cady et al., 2003). Besides the requirement of multiple lines of evidence for assessing elusive traces of microbial life, their tracking in the precious samples to be returned from Mars also necessitates optimized nondestructive methods as a priority. In this respect, advancing the investigation of traces of ancient microbial life on Earth using nondestructive, multiscale, and multiprobe approaches therefore represents a fundamental step in preparations for the investigation of samples returned from Mars (Kminek et al., 2022).

To address these analytical challenges, we combined conventional methods and state-of-the-art X-ray synchrotron nanoimaging in a multiscale and multiprobe study of microfossiliferous Rio Tinto rock samples. We explored methods well-known in geobiological studies, such as Raman microscopy, electron probe microanalysis (EPMA), scanning electron microscopy (SEM), and time-of-flight secondary ion mass spectrometry (ToF-SIMS). To push the limits of analysis to nanoscale and ultra-trace chemical levels, we combined synchrotron nano-X-ray fluorescence with 3D micro-to-nanoimaging ptychographic X-ray imaging in a setup adapted to laterally extended samples, such as petrographic thin sections.

Ptychography, a cutting-edge X-ray nanoimaging technique (Dierolf et al., 2010; Pfeiffer, 2018), offers a remarkable avenue for the non-destructive investigation of materials with subtle absorption contrast, including minerals (De Boever et al., 2015) and microfossils (Maldanis et al., 2020), which enables their three-dimensional characterization based on quantitative electron density contrast. To overcome the limitations of preparing micrometric cylindrical samples and enable the investigation of larger areas, this method was developed in a setup for laminographic nano-imaging (See methods of Holler et al. (2019), which allows 3D imaging of laterally extended samples. This approach can improve the analysis of petrographic thin sections by simplifying sample

preparation and facilitating the exploration of multiple areas of interest over large field-of-views and with exceptional 3D nanometric resolution. In the present study, we employed Ptychographic X-ray Computed Laminography (PyXL) to delve into the rich microfossil diversity of Rio Tinto, taking a comprehensive multiscale approach to unravel the intricate details of individual fossils within their geological and environmental contexts.

1.1. Geologic and petrographic context

The analyzed samples were derived from ferric oxyhydroxide deposits of the Rio Tinto Upper Terrace in the Alto de La Mesa region (Fig. 1). These beds were formed during the early Pleistocene due to the interaction between alternating acidic fluvial and lacustrine conditions fueled by acidic springs that originated from the bio-oxidation of the Cerro Salomon and Cerro Colorado pyritic ore bodies (Fernández Remolar and Knoll, 2008). The entire stratigraphic section (Fig. 1a) exhibits a diverse range of sedimentary facies with varying levels of ferric mineralization in detrital layers. The upper sequence (Fig. 1b) commences with conglomeratic and sandy deposits cemented by iron oxysulfates and oxyhydroxides (Fernández Remolar et al., 2005), culminating in chemically precipitated sediments.

Our main sample originates from the highest part of a shallowing upward sequence (Fig. 1c), characterized by the

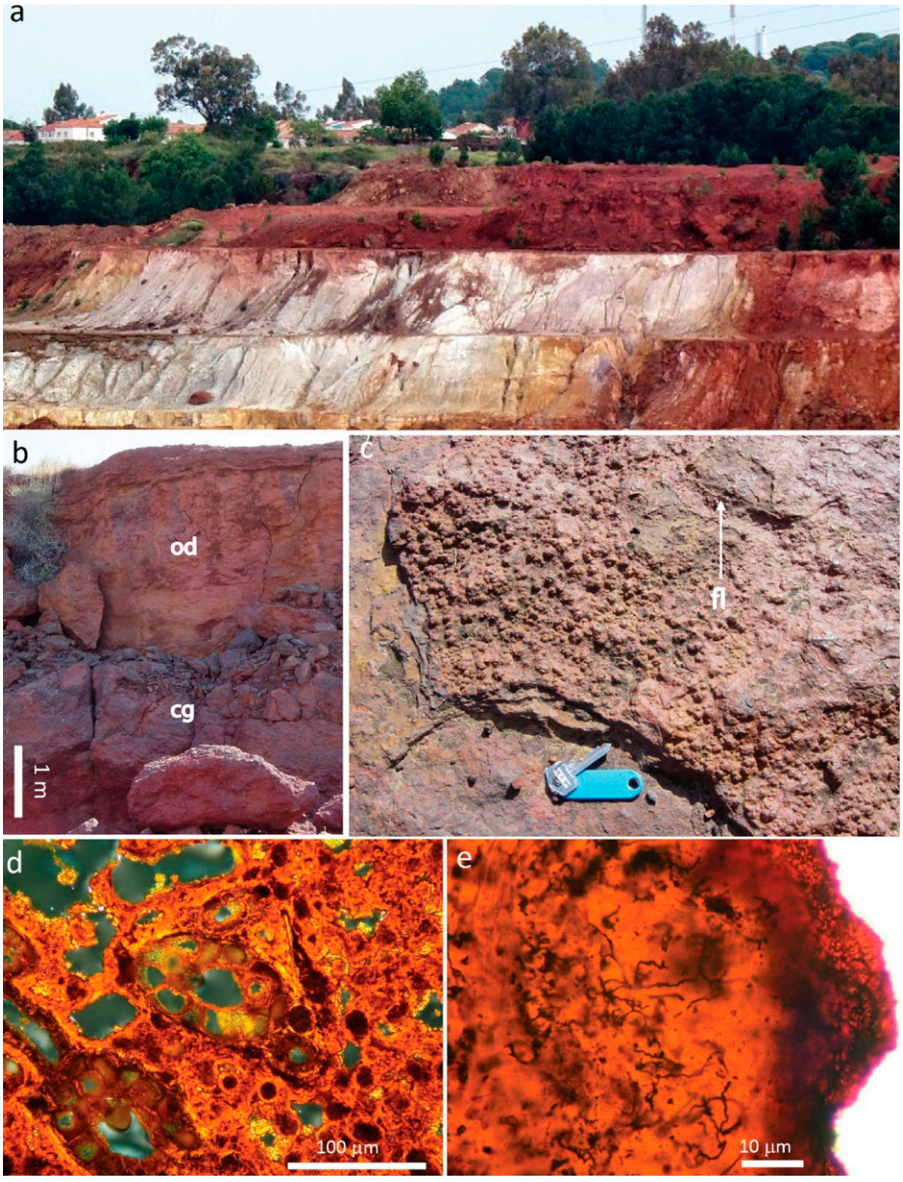

FIG. 1. Geological context of the 2.1 Ma Upper Terrace of Rio Tinto in the Alto de la Mesa location from where the sample was collected. **(a)** General view of the reddish Upper Terrace covering a highly whitish weathered shale to kaolinite. **(b)** Detail of the >5-m-thick upper sequence starting with conglomerates (cg), followed with oxyhydroxide deposits (od) with varying content in detrital materials and plant debris. **(c)** Topmost of a shallowing sequence in the Upper Terrace consisting of oxyhydroxide popcorn pseudomorphs replacing original copiapite and containing thin laminated deposits with microbial filaments. **(d)** Thin section of the upper oxyhydroxide deposits showing mineralized plant debris. **(e)** Bacterial branched filaments preserved inside a cryptocrystalline mineral matrix.

accumulation of thin laminar deposits. These deposits formed through primary sedimentary processes that generate a seasonal pattern of precipitation and the mineralization of ferric compounds in the acidic river and ground waters. Specifically, the ferric compounds present include nano-phase goethite and jarosite. During summer months, these compounds undergo recrystallization and transform into goethite and even hematite (Ferna et al., 2003; Fernández Remolar et al., 2005). As diagenesis progresses over time the goethite content of the sedimentary rocks increases, which eventually leads to hematite formation (Preston et al., 2011) from sulfate loss and mineral dehydration (Fernández Remolar, et al., 2021b). Consequently, microorganisms that reside in the deposits or penetrate the micro-laminar seasonal structures become preserved within a bulk or cryptocrystalline matrix of ferric oxyhydroxides/oxysulfates. During diagenesis, these matrix materials transform into hematite and goethite, with residual traces of sulfates (Fig. 1e) (Fernández Remolar et al., 2005; Fernández Remolar and Knoll, 2008).

Petrographic analysis revealed that the rock comprises a cryptogranular matrix of iron oxyhydroxides (goethite and hematite), with a high density of voids and fenestral structures crosscut by filaments (Fig. 1d, e). Such a fabric suggests that the sediment had a high input of plant debris and other biological components from macro-organisms, which were later degraded by fungi and bacteria (Fernández Remolar and Knoll, 2008). Filaments occur as clusters of two to five specimens with brownish color, variable length, and elongated or twisted morphology (Fig. 2a, Fig. 3a, Supplementary Fig. S1, Fig. S2). Under optical microscopy, the filaments appear inside >10-micron massive layers to <5-micron-thick lamina stacks of cryptocrystalline goethite (Fig. 2a, Fig. 3a). The lack of transparency of hematite impedes the recognition of filaments inside this mineral, if present. Other mineral structures of unknown composition have a dark brownish color and are clearly visible amid the translucent orange of the goethite matrix.

2. Materials and Methods

2.1. Sample selection and preparation

All analyses were performed on sample AM3-3/c that was collected at the lower part of the 10-m-thick section of the Rio Tinto upper terrace in the Alto de la Mesa location (Fernández Remolar and Knoll, 2008). The upper terrace has been assigned to the late Pliocene in age, around 2.0 ± 0.1 Ma (Fernández Remolar et al., 2005). The sample was sawed using a diamond blade and polished for a microprobe grade analysis using a 0.3 μm alumina paste to reduce surface imperfections. The selection of the filaments of interest was done by petrographic analysis of the thin section under optical microscope.

2.2. Nano X-Ray fluorescence

We carried out nano-X-ray fluorescence (XRF) analysis for mapping the distribution of elements (Z > Na) within the filaments and their surrounding environment. Nano-X-ray Fluorescence (nano-XRF) lower-resolution maps were acquired directly on petrographic 15 μm-thin sections at the beamline CARNAÚBA (Tolentino et al., 2023), Sirius synchrotron, Brazil. Experiments were carried out at the TARUMÃ station, with a 9.75 keV monochromatic beam KB-mirror focused at 300 nm × 300 nm. Full XRF spectra were collected using two Vortex four-element silicon drift detectors.

For the higher resolution nano-XRF, filaments from the same thin section were extracted in 1–2 μm thick lamellae by Ga-focused ion beam under an SEM (FIB-SEM). Samples were prepared at TESCAN Analytics using Ga beams of 30 kV for the cuts, followed by grazing Ar 5 kV beams for sample curtaining removal and Ga surface cleaning. Elemental maps were obtained at the ID16B beamline of ESRF-EBS where spectra are collected in continuous scanning mode, by raster-scanning the sample in front of the focused beam while detectors continuously collect spectra. Detectors used are 3 elements Hitachi Vortex-ME3 SDD 3 × 50 mm^2 and 7 elements MIRION SDD 7 × 50 mm^2 connected to XIA xMAP pulse processing electronics. Using the "pink" beam mode (full undulator harmonic), flux used was 5 × 10^{11} ph/s at 17 keV and dwell time was 100 ms.

2.3. Ptychographic X-ray laminography

For the PyXL, regions of approximately 3 × 3 mm^2 containing filaments were cut from the petrographic thin section with a diamond saw blade. The rock sections were attached to glass with nonremovable epoxy, so the glass was polished down until sample achieved a final thickness of 30 μm. The PyXL was performed with the laminography nanoimaging instrument (Holler et al., 2019) at the cSAXS beamline of the Swiss Light Source at the Paul Scherrer Institut, Switzerland. A photon energy of 6.2 keV was selected using a double-crystal silicon monochromator. Sample was positioned at an angle θ = 61° with respect to the beam propagation direction, and scan points followed a Fermat spiral trajectory. The first sample (ROI 1) was scanned in a far-field ptychography configuration, with sample positioned downstream of the focal position, with a beam diameter of 4 μm. An FOV in the sample plane of 85 μm × 85 μm was scanned with a step size of 2.2 μm following the Fermat spiral trajectory and exposure time of 50 ms per point. A total of 1800 projections were obtained spanning 360° with an angular step of 0.2°. The second sample (ROI 2) was scanned in a near-field ptychography configuration, with sample positioned 5.2 mm downstream of the focal position and beam diameter of 50 μm. An FOV in the sample plane of 180 μm × 180 μm was scanned with a step size of 5 μm and exposure time of 100 ms per point. A total of 2000 projections were obtained with angular step of 0.18°.

The complex-valued laminography projections were reconstructed using an area of 320 × 320 pixels of the Eiger photon-counting detector placed 5.234 m downstream of the samples. For the far-field PyXL, reconstruction was performed using 300 iterations of the difference map (DM) algorithm (Thibault et al., 2008) followed by 300 iterations of a maximum likelihood (ML) refinement (Thibault and Guizar-Sicairos, 2012), which resulted in a pixel size of 43 nm. For the near-field PyXL, 2000 iterations of the DM algorithm that followed the ML refinement were used, which resulted in a pixel size of 74.6 nm. All reconstructions were carried out using PtychoShelves (Wakonig et al., 2020).

Three-dimensional laminographic reconstruction was obtained after postprocessing and iterative alignment of the projections (Odstrčil et al., 2019) using a modified filtered backprojection method with the filtering kernel multiplied by

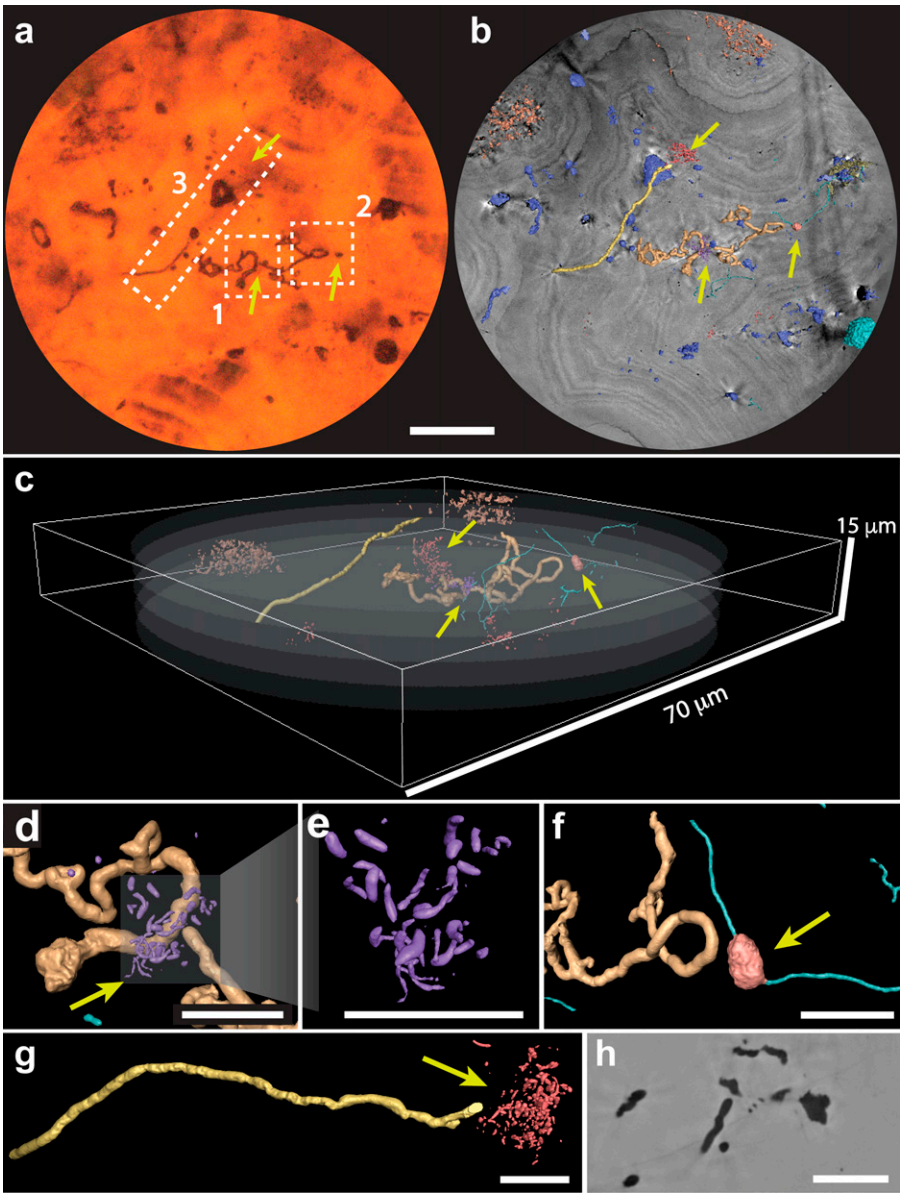

FIG. 2. ROI 1 imaged by PyXL showing different microbial structures. Yellow arrows indicate putative microbial structures revealed by PyXL and invisible in optical microscopy **(a)** Transmitted optical micrograph of the ROI 1 (~70 µm radius) showing twisted and elongated filaments within a cryptocrystalline goethite matrix. **(b)** Same FOV of **a** observed in a PyXL virtual slice with the visible structures rendered in 3D. The botryoidal laminations surrounding the filaments are visible as darker pixel intensities. **(c)** Three-dimensional lateral view of the ROI 1 showing the distribution of the microbial structures within the sample volume. **(d–g)** Detailed views of the regions outlined in (**a. d**) outlined region 1 showing submicrometric rod-like structures associated with filaments. **(e)** Detailed view of the rod-like structures. **(f)** Outlined region 2 showing a thicker filament (visible in **a**) near a thinner filament with a spheroidal nodule (not visible in **a**). **(g)** Elongated filament (visible in **a**) and closely associated rod-like structures. **(h)** Detail of a virtual laminographic slice showing crosscuts of the filaments, composed of a void-like, low-density material phase, with no other minerals associated. Scale bars: a–b: 20 µm, and d– f: 5 µm. PyXL, ptychographic X-ray computed laminography.

$\sin(\theta)$ to account for the laminography geometry (Helfen et al., 2011).

The pixel intensity (in gray level) on the laminographic virtual slices is related to the electron density of the structure, that is, features that appear darker in the virtual slices present lower electron densities than those appearing brighter (Fig. 2b,h, Fig. 3b,h,j,l). However, the laminographic setup leads to a missing cone of information in reciprocal space during reconstruction, which can cause halos and prevent this electron density to be estimated quantitatively, contrary to PXCT (Holler et al., 2019; Maldanis *et al.*, 2020). PXCT was able to distinguish organic material (i.e., kerogen) from air voids and quartz matrices in Precambrian microfossils (Maldanis et al., 2020). Due to its relatively recent development, it is still to be determined whether PyXL would allow the discrimination of low-density material phases

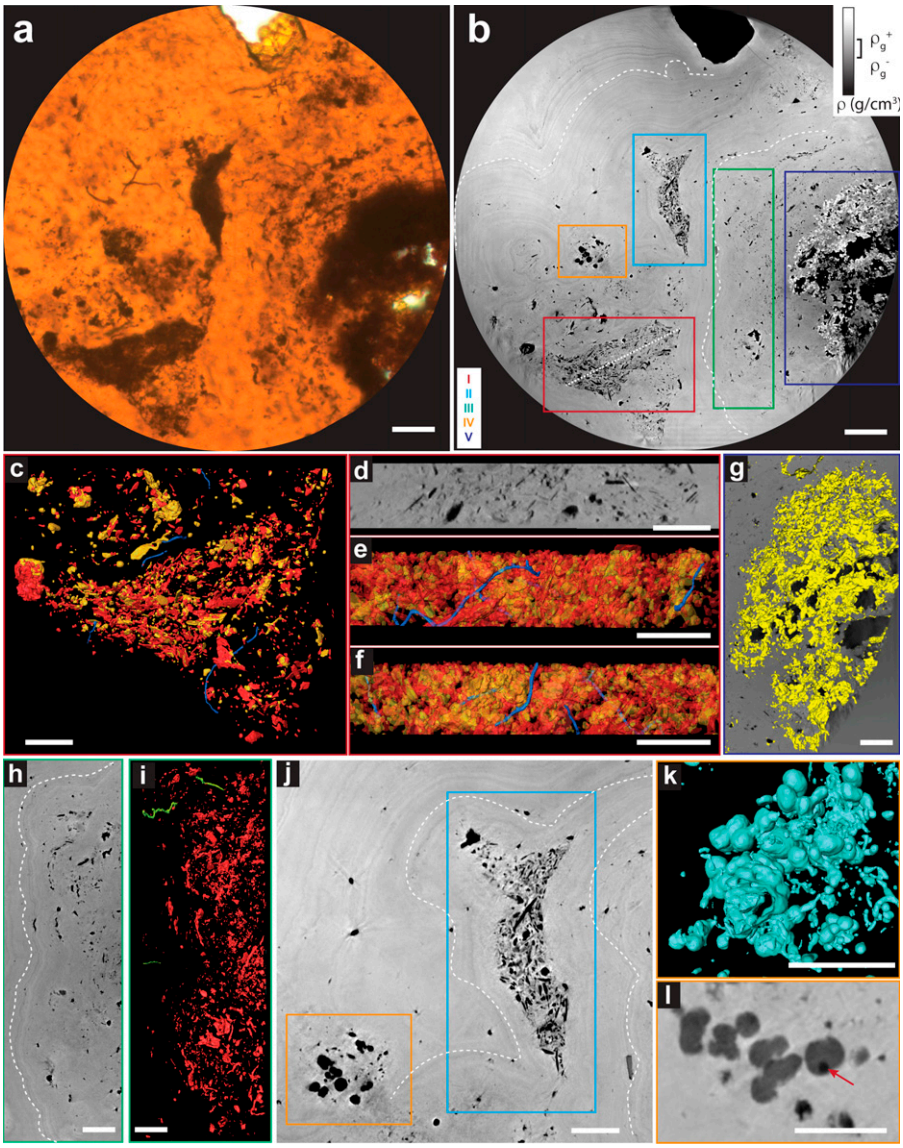

FIG. 3. Diversity of structures observed in ROI 2**. (a)** Transmitted optical micrograph of the ROI 2 ($\sim$ 180 μm) that was imaged with PyXL. Filaments and other features are dark brownish structures, contrasting with the orange goethite matrix. **(b)** PyXL 3D virtual slice showing ROI 2 with the regions I-IV outlined in different colors. The gray level is directly related to electron density, indicating that most of the darker structures seen in **a** are lower in density than goethite (matrix) (ρ_g 3.3–4.3 g/cm^3 tabulated values), apart from the high-density area on region V (brightest intensity) likely corresponding to a hematite composition. Botryoidal laminae of goethite are visible as light and dark sequences, with shapes enhanced by the dashed lines. **(c)** Three-dimensional rendering of features from the region I, showing the agglomerate of platy crystals and some associated filaments. **(d)** Detail of cross-sections of region II (dashed line in **b**) and **(e–f)** 3D rendering of the structures showing filaments crossing the layer of particles. **(g)** 3D rendering of the high-density structures from region V superposed with a PyXL virtual slice. The high-density crystals surround low-density (dark pixels in the gray-level virtual slice) areas, probably holes in the rock matrix. **(h)** Virtual slice of region IV showing botryoidal laminations and low-density structures rendered in 3D in red in **i,** as well as some cross-cutting filaments (in green). **(j)** Detail of the virtual slice showing regions II and III. Dashed lines mark the shape of the botryoidal lines that seem to push and shape the cluster of structures. **(k)** Three-dimensional rendering of the spheroidal structures from region III and **(l)** detail of these spheroids in the virtual slice showing their low-density, nonhollow morphology. The red arrow points to a nucleus of lower density within one of the spheroids. Scale bars: 20 μm in a–b and 10 μm for c–l.

such as air and organics. Further studies simulating the effects of the missing cone of information on organic filamentous biomorphs compared to casts could resolve this matter and contribute to the understanding of the limits of this imaging method.

2.4. Image analysis

Images were segmented using gray level values thresholding on the software Avizo (Thermo Scientific™). Filaments were identified among other structures of similar electron density (gray level values) based on their morphology in 3D.

To obtain a reproductive process for quantitative morphometric analysis of all the filaments, we refined their segmentation using the following procedure: a morphological operator of dilation was applied to obtain the matrix surrounding the filaments. Within this new mask, seeds for watershed were generated for the filaments (based in the lowest pixel intensity) and matrix (based in higher pixel intensity and pixels furthest away from the filaments). Watershed segmentation process was then applied to define the border between filament and matrix, and the result was visually inspected for removal of artifacts. The labels were refined using the Smooth Labels function with a kernel size of 5 pixels. The diameter of the filaments was determined with the Euclidean distance transform algorithm using the BoneJ plugin on ImageJ (Doube et al., 2010), which provides mean thickness values, standard deviation, and maximum values. The thickness image maps were generated in Avizo, using the Thickness Maps function.

3. Results

3.1. On the preservation of microbial traces

Investigations at the subcellular scale of individual filaments provide a deeper understanding of the composition and means of preserving these microbial traces. Despite the poor preservation potential described for acidic terrains (Sumner, 2004), the microfossils exhibit an exceptional three-dimensional level of morphological preservation, which shows cylindrical shapes even for the thinnest specimens (< 500 nm). The relative electron density of the filaments' intracellular volume, observed in the PyXL virtual slices (Fig. 2a, b, h, Suppl. Figs. 1a–c, 2d), indicates a material phase less dense (darker pixels) than the matrix, which is composed of goethite (*i.e.*, < 3.3 g/cm^3) (Fig. 3b, Supplementary Fig. S3).

Furthermore, no variations in intensity were detected within the low-density material phase that composes the filaments, which indicates no preservation of cell envelopes or intracellular structures. No denser minerals, such as hematite or pyrite, were observed within the structures or on their outer surfaces (Fig. 2h, Supplementary Fig. S1c, Sf, Supplementary Fig. S2d, Supplementary Fig. S4). Further analysis at the micrometric scale with Raman and ToF-SIMS did not detect organic contents directly associated with filaments (Supplementary Fig. S3, Supplementary Fig. S5). Such features, which are suggestive of hollow structures, are consistent with preservation as microbial casts or microborings.

Detailed chemical analysis of individual filaments was carried out with high-resolution synchrotron nano-X-ray fluorescence with 50 nm resolution. Despite the minute detection limits of the analysis using high photon fluxes and reduced sample thickness (see Methods) (Lemelle et al., 2017), filaments do not show any particular metal signatures. They are, however, depleted in Fe and enriched in Ar, an atmospheric element which reiterates that the structure is hollow, and therefore filled with atmospheric gases (Fig. 4). The matrix contains substantial and homogeneous Fe content while displaying lower amounts of V, Cr, Cu, Zn, As, Rb, Pb, and spots of Ca.

3.2. Inferring a microbiota from qualitative and quantitative morphology

Two filamentous regions were selected in a petrographic thin section for 3D imaging at the nanoscale with PyXL (ROI 1—Fig. 2 and Supplementary online data and ROI 2—Fig. 3). Virtual 3D volumes of filaments and other structures were reconstructed for qualitative and quantitative analysis. The filaments display a tubular shape, without large variations in diameter such as flattened or widened regions. Besides filaments observable under the optical microscope, 3D nano-images reveal a more diverse association of microbial structures (Fig. 2b–g), including rods and spheroids. Many of these could not be observed through conventional microscopy because of their small (submicrometer) size and surroundings of opaque minerals.

Quantitative morphometric analysis enabled us to recognize the following three distinct filamentous morphotypes, distinguished by cross-sectional diameter (Fig. 5, Supplementary Table S1): morphotype 1 (∅ ~ 750 nm, Fig. 5a–c), morphotype 3 (∅ ~ 500 nm, Fig. 5d, e), and the gracile morphotype 2 (∅ ~ 240 nm, Fig. 5f–h). Regular variations in diameter suggest septation and, therefore, cells rather than simply extracellular sheaths in some specimens (Fig. 5b, c, h).

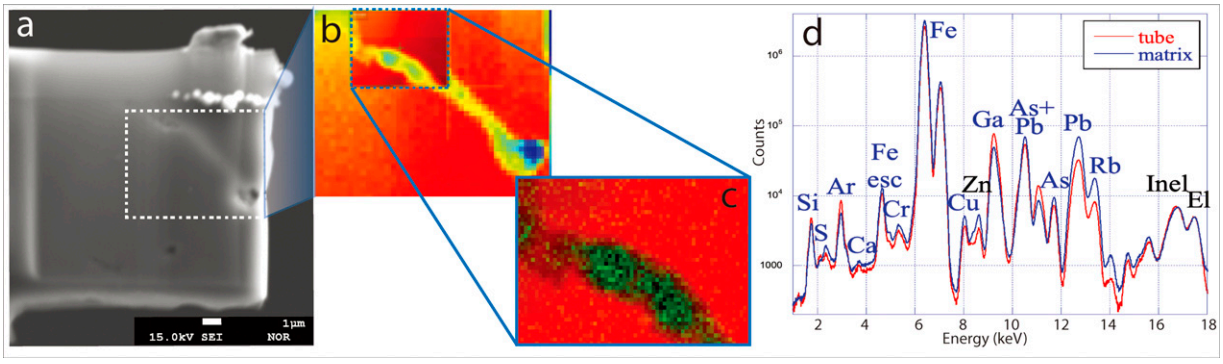

FIG. 4. Nano-XRF analysis of individual fossil filaments. **(a)** SEM image of the FIB sample showing the filament analyzed by nano-XRF. **(b)** X-ray attenuation map of the area analyzed by XRF showing the full filament morphology and the area selected for high-resolution mapping. **(c)** High-resolution map showing Fe (red) distribution in the matrix and Ar (green) filling the filament area. **(d)** XRF spectrum of tube and matrix, normalized to number of pixels. Besides Ar (from air) and Ga (deposited during the FIB preparation), the tube has no elemental signature different from the matrix. SEM, scanning electron microscopy; XRF, X-ray fluorescence; FIB, focused ion beam.

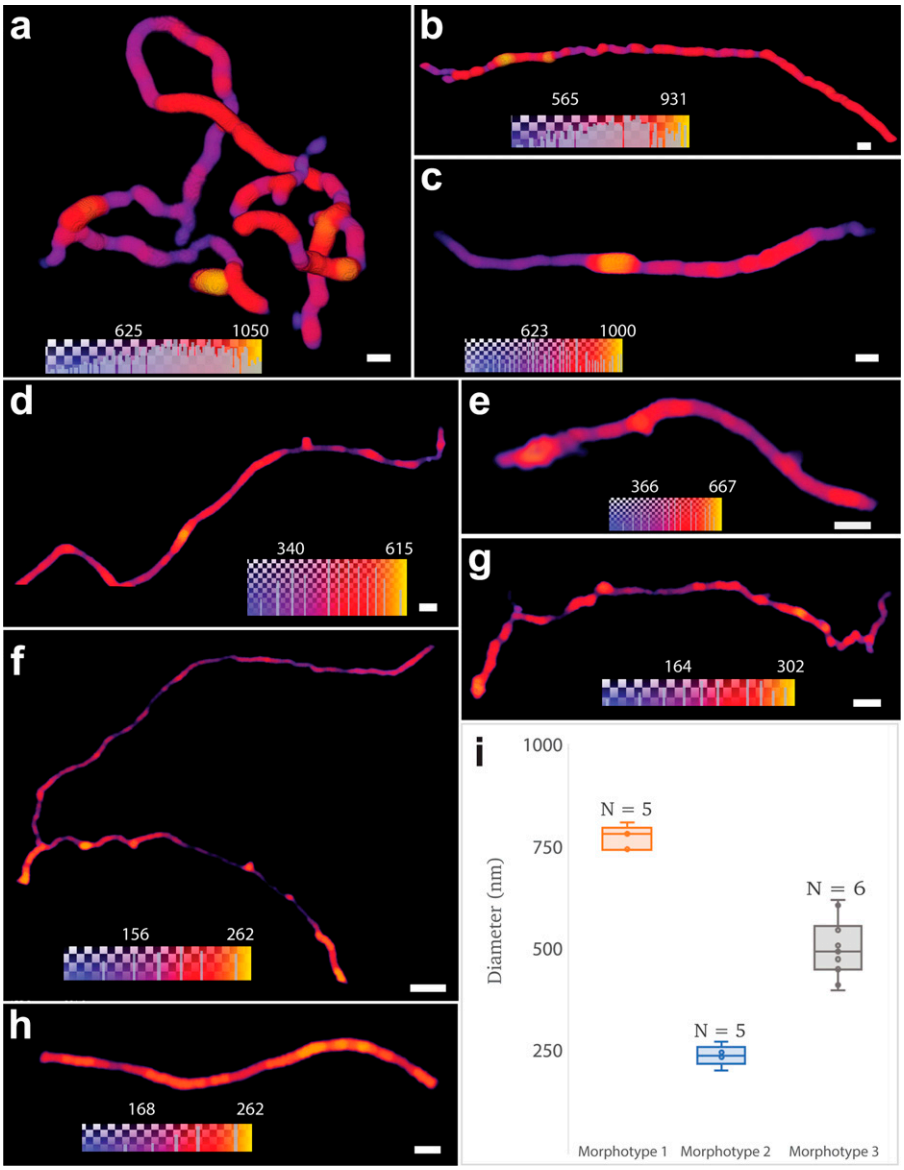

FIG. 5. **(a–h)** Three-dimensional thickness map of distinct filaments detected in ROI 1 and ROI 2 from Rio Tinto using PyXL segmented data. The colormap refers to the diameter values written above the colors. The gray vertical lines within the colormap correspond to a frequency histogram for the diameter values. **(a–c)** Morphologies with thicknesses exceeding 700 nm (morphotype 1) present in ROI 1 **(a, b)** and ROI 2 **(c)**. **(d–e)** Filaments in ROI 2 ranging from 400 to 600 nm (morphotype 3). **(f– h)** Filaments measuring less than 300 nm (morphotype 2) in ROI 1, previously unnoticed in optical microscopy. **(i)** Box plots, showing filamentous structures' thickness ranges, suggest the presence of three distinct microbial populations. Scale bar: 1 μm.

Morphological analysis can be taken a step further by describing filaments' anatomy, folding levels, ramifications, and relative distributions. In morphotype 1, for example, both frequently bending and looping (Fig. 2c–d, f, Fig. 5a) or roughly linear filaments are observed (Fig. 2g, Fig. 5b, c). In both cases, the filaments show short ramifications that form hooks or loops (Fig. 2d, f, g). In contrast to the thick filaments, the gracile filaments of morphotype 2 lack loops but can exhibit extensive ramification (Fig. 5f). One was observed to encompass a nodular structure (Fig. 2f). Morphotype 3 filaments display a sinuous morphology (Fig. 5d, e) and commonly crosscut mineral layers (Fig. 3c–f, Supplementary Fig. S6). Besides the filamentous morphotypes, rod-shaped nanostructures are scattered in 5–10 μm wide clusters, congregating around the filaments (Fig. 2d–e, g).

The complexity of these morphotypes and, in particular, the ramified filaments can be compared with the morphological traits of various groups of the branched Actinobacteria abundantly found in the Rio Tinto subsoil (López-Archilla, Marin and Amils, 2001). The life cycle of these microorganisms includes several stages with very different filamentous morphologies. In the vegetative stage, the substrate and aerial hyphae are more or less branched, which would explain the observed morphologies. The nodular structure (Fig. 2f) resembles reproductive structures or stress-induced cells in Actinobacteria (Li et al., 2016; Ramijan *et al.*, 2018). Some

species or even spores of these microorganisms can also display a rod-shaped morphology, such as the rod-shaped structures observed to be closely associated with filaments (Fig. 2d, e, g).

In summary, this unique 3D multiscale nanoimaging allows us to probe the structural complexity of dozens of individuals, some being invisible or hidden by other structures in optical microscopy, at the scale of hundreds of micrometers, with a resolution on the order of 100 nm. This allows straightforward statistical analysis and, thus, the identification of three distinct filamentous morphotypes. The level of morphological complexity revealed enables us to support the hypothesis that multiple species consistent with Actinobacteria are preserved in Rio Tinto rocks.

3.3. Ecological and metabolic inferences from multiscale imaging

Inferences about ecology can be challenging, but in the first instance, helpful information can be derived by determining relative population sizes and spatial distributions of observed morphotypes in the sediments. PyXL provides a multiscale view, which encompasses larger circular fields-of-view with 70 μm (Fig. 2) and 180 μm diameters (Fig. 3). The textural views were complemented by chemical information obtained from synchrotron nano-X-ray fluorescence maps and EPMA (Supplementary Fig. S7, Supplementary Fig. S8, Supplementary Fig. S9).

The close association of filamentous morphotypes I and II with rod-shaped structures (Fig. 2) points to an assemblage of at least two to three different species. These specimens have no preferential orientation and transect light and dark alternating laminae of the matrix, characteristics of botryoidal goethite.

Filaments of morphotype III are also observed within tightly packed particle clusters of blob and platy morphologies (I and II in Fig. 3b, j and Fig. 3c–f). These particles are Fe-depleted, with Ti-rich spots (Supplementary Fig. S7b, c). They are less dense than goethite and seem to be markedly pinched by Fe-richer goethite botryoidal laminae (Fig. 3b, j, Supplementary Fig. S7b). Within these clusters, filaments also show no preferential orientation and exhibit a sinuous aspect. They are never transected by the larger mineral particles (>5 μm) with which they are closely associated (Supplementary Fig. S6).

Filaments are also observed in a region of texture intermediate between the botryoidal lamination and cluster textures (III in Fig. 3b, Supplementary Fig. S10c, d). A region that is thinner and less dense than the abovementioned particle clusters shows anhedral structures of varied morphologies and sizes that follow the topology of the botryoidal goethite laminae (Fig. 3h, i, Supplementary Fig. S10c–d). It shows spots depleted in Fe and rich in Ti (Supplementary Fig. S7b,c).

The distribution of these filaments within the rock texture provides valuable insights about ecological and taphonomic aspects. The observed clusters, pinched between the botryoidal laminations, indicate that the growth of the botryoidal goethite caused their displacement and rearrangement. Within this framework, the intermediate texture could represent degraded organic material from partially displaced mats during the formation of botryoidal lamination. The exceptional three-dimensional preservation of filaments within the botryoidal laminations, as well as within the cluster of particles, suggests that they could not have been present before the spatial reconfiguration of these textures. Instead, these microbial structures could only have been preserved after the rearrangement of the clusters and intermediate textures and during or after the formation of the botryoidal goethite. These filaments could be interpreted as casts or microborings created by chemoheterotrophic bacteria that perforate sediments by reducing Fe^{3+}-bearing minerals. This process has been identified as a significant driver of carbonate precipitation in the Rio Tinto (Fernández-Remolar et al., 2012). It can be mediated by Actinobacteria (González et al., 2020), a group containing abundant endolithic microbes (Sajjad et al., 2022) that are also abundant in the Rio Tinto host rock underground (Amils et al., 2023). The presence of goethite laminations that concentrate organics (Supplementary Fig. S5, Supplementary Fig. S8, Supplementary Fig. S9) is attractive to endolithic microbes, as they oxidize organic matter. This would explain the presence of most filaments within these textures.

Aggregates of contact or near-contact globular and dumbbell structures with diameters ranging from submicron to approximately 3 μm were identified (Fig. 3j–i, Supplementary Fig. S10e–h). These are nonhollow, with a density lower compared with the goethite matrix, and are depleted in Fe and Cu and slightly enriched in Ca (Supplementary Fig. S7), which is consistent with microbially mediated carbonates previously observed at Rio Tinto (Sánchez-Román et al., 2007). Their formation is thought to reflect the activity of heterotrophic microbes that couple the reduction of Fe^{3+} to the oxidation of organic compounds (Fernández-Remolar et al., 2012). Some spherical structures display inner spots of lower density (darker areas pointed in Fig. 3i). The possible presence of microorganisms nucleating these crystals calls for further investigations.

An Fe-rich texture denser than goethite is observed surrounding voids in the mineral matrix (Fig. 3g, Supplementary Fig. S7b, Supplementary Fig. S10 a,b,). It is consistent with hematite, which could have formed locally by the circulation of fluids through the voids. No filamentous structures were preserved in this mineral texture, which suggests that the hematite formation might have been sufficiently disruptive to erase biological traces.

4. Discussion

4.1. Assessing biogenicity from microstructures

Our Rio Tinto study illustrates some of the analytical challenges potentially expected for other extreme environments, including Noachian–Hesperian rocks on Mars. The submicrometer size of the Rio Tinto microfossils, associated to their low organic content within a Fe-rich matrix, poses problems for the colocalization of morphological traces and organic compounds using classical methods, such as micro-Raman, EPMA, and ToF-SIMS. Discerning whether possible organics traces are present below the detection levels of these methods or whether these structures represent casts would require nanoscale analytical methods with sensitivity down to ultra-trace levels. Our nano-X-ray Fluorescence (XRF) analysis confirmed the absence of metal signatures associated with the filaments, discarding possible preservation of metallome elements (Hickman-Lewis et al., 2020). Nanoscale analysis

of the metal contents down to ultra-trace levels did not identify any elemental signature suggestive of the preservation of a cell envelope or intracellular features and instead revealed the empty-cast nature of the microfossils. This finding supports the hypothesis that only goethite or its precursor iron precipitates played a major role in preserving these fossilized structures. During diagenesis, possible original organics, including potential cell-wall remnants, would undergo leaching and decay within the tubes. Other studies suggest that these organics could be eventually trapped and partially preserved as biomarkers within the surrounding matrix (Fernández Remolar, Carrizo, et al., 2021a; Fernández Remolar, *et al.*, 2021b).

The colocation of organics and microbial structures, particularly if indicating the preservation of a cell envelope enclosing a hollow structure, is often regarded as a reliable criterion for supporting the biogenicity of putative microbial fossils (Buick, 1990; McMahon and Jordan, 2022; William Schopf *et al.*, 2010). However, this cannot be applied to structures preserved as casts or molds, such as in Precambrian rocks (Dodd et al., 2017) and hydrothermal deposits (Parenteau and Cady, 2010; Little *et al.*, 2021). Despite the lack of organic envelopes, the multiscale examination of 3D morphologies of Rio Tinto microstructures provides a suite of converging and mutually supportive indications of their biogenicity. By imaging large volumes that contain multiple specimens, aspects related to the occurrence, abundance, and behavior of the microorganisms were obtained: the different filamentous morphotypes are immersed in the rock matrix and coexist in an abundant, multispecies assemblage. They are also closely associated with other rod-shaped, possibly microbial structures or microbial remains, supporting a community-like structure. Details of morphology down to the nanoscale reveal several characters that are also supportive of their biogenicity, such as (a) sizes compatible with bacterial morphologies, (b) morphometry differences that suggest multispecies assemblages, (c) consistency of cross-sectional cylindrical shapes along the entire lengths of the filaments (*i.e.*, absence of flattened or largely deformed areas), (d) narrow range of diameter within individual specimens, (e) hollow structures, and (f) signs of taphonomical degradation. The possibility of combining these micro- and nanoscopic traits with the ecological and mineralogical contexts of many specimens strengthens the interpretation of their biogenicity. This multiscale approach also elucidates taxonomic, taphonomic microbial–mineral interactions associated with the Rio Tinto microbiota. Filaments are interpreted as casts or microborings of chemoheterotrophic bacteria, possibly belonging to the diverse group Actinobacteria. Then, as now, local primary producers included land plants and algae, preserved locally in Rio Tinto terraces (Fernández Remolar and Knoll, 2008). Extending the exploration and analysis of microfossiliferous rocks from petrographic optical microscopy to 3D multiscale nano-imaging by PyXL brings important advances in the study of fossil biosignatures. In particular, it enhances the possibility of obtaining 3D ultra-cellular morphological information for a large number of specimens, and under different mineral settings, even when they are invisible to optical microscopy.

4.2. X-ray analytical methods in the context of extraterrestrial samples

The search for microfossils in 2.1 Ma iron-rich fossiliferous samples of Rio Tinto illustrates the essential role of laboratory state-of-the-art techniques to diagnose challenging microbial traces compared to portable instruments already deployed or planned for Mars missions (Azua-Bustos et al., 2023). Novel state-of-the-art synchrotron X-ray 2D and 3D nanoimaging provides highly sensitive probes that are nondestructive while penetrating deeply into the substrate. Such capabilities can provide decisive information at several stages of the analytical chain deployed to search for life traces.

Combinations of tomographic techniques with hard X-rays have been explored in recent decades for the purpose of detecting signs of aqueous alteration in submillimeter rock samples, potentially even when confined within a container such as a tube returned from Mars (Lemelle et al., 2003, 2004, 2007). Because water is essential for life, these methods would be advantageously applied during the initial examination phase to identify rock samples that exhibit indications of water infiltration.

Hard X-ray nanoimaging is also uniquely able to probe complete microfossils embedded in opaque rocky matrices. Nano-XRF imaging relies on the detection of trace contents of the elements of high atomic number (Z). This nanoscale imaging necessitates scaling down the sample size to match that of the microorganisms themselves (Cavalazzi et al., 2021; Lemelle *et al.*, 2017). Other methods such as scanning transmission X-ray microscopy have been explored for obtaining chemical speciation and distribution of light elements at the nanoscale (Cosmidis et al., 2013; Miot, Benzerara and Kappler, 2014). These soft X-ray methods require samples to be reduced to thicknesses in the nanometer range and offer valuable insights into the intricate structures and elemental composition of microbial systems, enhancing our understanding of their unique characteristics.

The advancement of coherent X-ray imaging techniques in synchrotron sources, particularly those based on quantitative electron density contrast, can bring important perspectives to nanopaleontology. Methods such as ptychographic X-ray computed tomography (PXCT) (Holler et al., 2014) offer a unique possibility for distinguishing organic and mineral phases within full specimens nondestructively in 3D, advancing the understanding of microfossils' composition and taphonomic processes at the nanoscale (Maldanis et al., 2020). These techniques would be advantageously applied before the analyses that involve the preparation of electron-transparent samples, which typically involve irreversible and destructive sampling of microfossils.

PyXL nanoimaging (Holler et al., 2019) applied in this study also extends the possibility of imaging microfossils directly within petrographic thin sections. This also allows the exploration of multiple areas of interest accessible over millimeter-scale areas, with a field of view of up to hundreds of micrometers and nanometric resolution. A drawback compared to PXCT is the lack of quantitative electron density. In a thorough and comprehensive analytical strategy, this method can be applied on rock thin-sections, bridging a gap in resolution and field-of-view that currently exists between optical and electron-based methods.

In addition to resolution, the effectiveness of an imaging method in distinguishing objects depends on the presence of sufficient contrast between the feature of interest and its background. In the case of visible light microscopy, contrast is derived from variations in intensity and color, as well as the

transparency of the matrix allowing for light transmission. These factors collectively contribute to the successful visualization and differentiation of objects under examination, enabling researchers to explore intricate details within the sample. When studying iron-rich rocks such as Rio Tinto and potentially other similar formations, the presence of opaque iron-oxides, notably hematite, poses an additional challenge to the investigation of microbial fossils. The identification of these fossils is limited to regions where optically transparent minerals like jarosite and goethite are found. This challenge is likely to be encountered with hematite-rich samples from Mars as well, which reinforces the importance of 3D X-ray methods to conduct accurate examinations of microbial biosignatures.

5. Conclusions

The investigation of microbial biosignatures from extreme environments like Rio Tinto, as well as those preserved in some Precambrian rocks, poses considerable challenges. Overcoming these challenges, however, can provide insights into both the difficulties and the possibilities that will be entailed in the quest for ancient microbial signatures in martian rocks. To gain a deeper understanding and resolve these intriguing pieces of evidence, it is crucial to embark on comprehensive exploration that utilizes advanced and state-of-the-art imaging methods at multiple scales. This endeavor not only enhances our comprehension of ancient life on Earth but also serves as a stepping stone for the development of robust methodologies in the analysis of martian samples. By doing so, we hope to help pave the way for future discoveries and the development of analytical tools up to the task of probing astrobiological samples from Mars and potentially elsewhere that will, in time, be returned to Earth.

Acknowledgments

The authors acknowledge the Paul Scherrer Institut, Switzerland, for synchrotron beamtime at cSAXS beamline of the Swiss Light Source (SLS), the CNPEM, Brazil, for beamtime at Carnaúba beamline of Sirius, and ESRF, France, for beamtime at ID 16B. From TESCAN, the authors acknowledge Elodie Chauvet for ToF-SIM measurements and Amandine David for the FIB preparations. L.M., L.L., and A.S. acknowledge support by the French National Research Agency in the framework of the Investissements d'Avenir program (ANR-15-IDEX-02).

Authors' Contributions

A.S., L.L., D.F.R., and L.M. defined scientific strategy. D.F.R. carried out sample selection and petrography and treated ToF SIMs data. L.M. prepared samples and performed PyXL experiments with M.H. and M.G.S. L.M. treated data and generated images. A.S. and L.L. performed nanoXRF experiments and data treatment. M.M. conducted Raman experiments with A.S. and L.M. L.M., V.M., and A.S. conducted SEM and EPMA analyses. L.M. interpreted the results with the support of L.L. and D.F.R. L.M., L.L., D.F.R., and A.S. cowrote the article. All authors read and contributed to the final editing.

Availability of Data and Materials

The 3D rendering generated after segmentation of the data of sample ROI 1 is available for visualization in the Sketchfab repository (https://sketchfab.com/3d-models/sketch-surf3-85aafafc35854955b1e0359a9cd920fa). The remaining data that support the findings of this study are available from the corresponding author upon reasonable request.

Author Disclosure Statement

The authors declare no competing financial interests.

Funding Information

This research is part of the "Origin of Life" project of the Université Grenoble-Alpes, supported by a French National Research Agency grant in the framework of the Investissements d'Avenir program (ANR-15-IDEX-02) and Sprint Mobility Project, FAPESP/Université Grenoble Alpes 2019/23611-1, and National Key Research and Development Program of China (Grant No. 2021YFA0716100). Correspondence and requests for materials should be addressed to laramcp@hotmail.com.

Supplementary Material

Supplementary Data S1
Supplementary Figure S1
Supplementary Figure S2
Supplementary Figure S3
Supplementary Figure S4
Supplementary Figure S5
Supplementary Figure S6
Supplementary Figure S7
Supplementary Figure S8
Supplementary Figure S9
Supplementary Figure S10
Supplementary Table S1

References

Allwood AC, Walter MR, Burch IW, et al. 3.43 billion-year-old stromatolite reef from the Pilbara Craton of Western Australia: Ecosystem-scale insights to early life on Earth. *Precambrian Res* 2007;158(3–4):198–227; doi: 10.1016/j.precamres.2007.04.013

Amils R, Escudero C, Oggerin M, et al. Coupled C, H, N, S and Fe biogeochemical cycles operating in the continental deep subsurface of the Iberian Pyrite Belt. *Environ Microbiol* 2023; 25(2):428–453; doi: 10.1111/1462-2920.16291

Amils R, González-Toril E, Fernández Remolar D, et al. Extreme environments as Mars terrestrial analogs: The Rio Tinto case. *Planet Space Sci* 2007;55(3):370–381; doi: 10.1016/j.pss.2006.02.006

Amils R, Fernández-Remolar D, The Ipbsl Team, et al. Río Tinto: A geochemical and mineralogical terrestrial analogue of Mars. *Life (Basel)* 2014;4(3):511–534; doi: 10.3390/life4030511

Azua-Bustos A, Fairén AG, González-Silva C, et al. Dark microbiome and extremely low organics in Atacama fossil delta unveil Mars life detection limits. *Nat Commun* 2023;14(1):808; doi: 10.1038/s41467-023-36172-1

Buick R. Microfossil recognition in Archean rocks: An appraisal of spheroids and filaments from a 3500 M.y. old chert-barite

unit at North Pole, Western Australia. *Palaios* 1990;5(5): 441–459; doi: 10.2307/3514837

Cady SL, Farmer JD, Grotzinger JP, et al. Morphological biosignatures and the search for life on Mars. *Astrobiology* 2003;3(2):351–368; doi: 10.1089/153110703769016442

Cavalazzi B, Lemelle L, Simionovici AS, et al. Cellular remains in a ~3.42-billion-year-old subseafloor hydrothermal environment. *Sci Adv* 2021;7(29); doi: 10.1126/sciadv.abf3963

Colín-García M, Kanawati B, Harir M, et al. Detection of peptidic sequences in the ancient acidic sediments of Río Tinto, Spain. *Orig Life Evol Biosph* 2011;41(6):523–527; doi: 10.1007/s11084-011-9258-x

Cosmidis J, Benzerara K, Gheerbrant E, et al. Nanometer-scale characterization of exceptionally preserved bacterial fossils in Paleocene phosphorites from Ouled Abdoun (Morocco). *Geobiology* 2013;11(2):139–153; doi: 10.1111/gbi.12022

De Boever W, Diaz A, Derluyn H, et al. Characterization of composition and structure of clay minerals in sandstone with ptychographic X-ray nanotomography. *Appl Clay Sci* 2015; 118:258–264; doi: 10.1016/j.clay.2015.09.020

Des Marais DJ, Nuth IJA, Allamandola LJ, et al. The NASA astrobiology roadmap. *Astrobiology* 2008;8(4):715–730; doi: 10.1089/ast.2008.0819

Dierolf M, Menzel A, Thibault P, et al. Ptychographic X-ray computed tomography at the nanoscale. *Nature* 2010;467(7314): 436–439; doi: 10.1038/nature09419

Dodd MS, Papineau D, Grenne T, et al. Evidence for early life in Earth's oldest hydrothermal vent precipitates. *Nature* 2017;543(7643):60–64; doi: 10.1038/nature21377

Doube M, Kłosowski MM, Arganda-Carreras I, et al. BoneJ: Free and extensible bone image analysis in ImageJ. *Bone* 2010;47(6):1076–1079; doi: 10.1016/J.BONE.2010.08.023

Farley KA, Williford KH. Seeking signs of life and more: NASA's Mars 2020 mission. *Eos (Washington DC)* 2017; doi: 10.1029/2017EO066153

Fenton HJH. Oxidation of tartaric acid in presence of iron. *J Chem Soc, Trans* 1894;65(0):899–910; doi: 10.1039/CT8946500899

Ferna DC, Rodriguez N, Go F, et al. Geological record of an acidic environment driven by iron hydrochemistry: The Tinto River system. *J Geophys Res* 2003;108(E7):1–15; doi: 10.1029/2002je001918

Fernández Remolar D, Carrizo D, Harir M, et al. Unveiling microbial preservation under hyperacidic and oxidizing conditions in the oligocene Rio Tinto deposit. *Sci Rep* 2021a; 11(1):21543; doi: 10.1038/s41598-021-00730-8

Fernández Remolar D, Gomez-Ortiz D, Huang T, et al. The molecular record of metabolic activity in the subsurface of the Río Tinto Mars analog. *Astrobiology* 2021b;21(11): 1387–1405; doi: 10.1089/ast.2020.2431

Fernández Remolar D, Knoll AH. Fossilization potential of iron-bearing minerals in acidic environments of Rio Tinto, spain: Implications for Mars exploration. *Icarus* 2008;194(1): 72–85; doi: 10.1016/j.icarus.2007.10.009

Fernández Remolar D, Morris RV, Gruener JE, et al. The Río Tinto basin, Spain: Mineralogy, sedimentary geobiology, and implications for interpretation of outcrop rocks at Meridiani Planum, Mars. *Earth Planet Sci Lett* 2005;240(1):149–167; doi: 10.1016/j.epsl.2005.09.043

Fernández-Remolar DC, Preston LJ, Sánchez-Román M, et al. Carbonate precipitation under bulk acidic conditions as a potential biosignature for searching life on Mars. *Earth Planet Sci Lett* 2012;351–352:13–26; doi: 10.1016/j.epsl.2012.07.015

González D, Huber KJ, Tindall B, et al. Acidiferrimicrobium australe gen. nov., sp. nov., an acidophilic and obligately heterotrophic, member of the Actinobacteria that catalyses dissimilatory oxido-reduction of iron isolated from metal-rich acidic water in Chile. *Int J Syst Evol Microbiol* 2020;70(5): 3348–3354; doi: 10.1099/ijsem.0.004179

González-Toril E, Llobet-Brossa E, Casamayor EO, et al. Microbial ecology of an extreme acidic environment, the Tinto River. *Appl Environ Microbiol* 2003;69(8):4853–4865; doi: 10.1128/AEM.69.8.4853-4865.2003

Helfen L, Myagotin A, Mikulík P, et al. On the implementation of computed laminography using synchrotron radiation. *Rev Sci Instrum* 2011;82(6):063702; doi: 10.1063/1.3596566

Hickman-Lewis K, Cavalazzi B, Sorieul S, et al. Metallomics in deep time and the influence of ocean chemistry on the metabolic landscapes of Earth's earliest ecosystems. *Sci Rep* 2020;10(1):4965; doi: 10.1038/s41598-020-61774-w

Holler M, Diaz A, Guizar-Sicairos M, et al. X-ray ptychographic computed tomography at 16 nm isotropic 3D resolution. *Sci Rep* 2014;4:3857; doi: 10.1038/srep03857

Holler M, Odstrcil M, Guizar-Sicairos M, et al. Three-dimensional imaging of integrated circuits with macro- to nanoscale zoom. *Nat Electron* 2019;2(10):464–470; doi: 10.1038/s41928-019-0309-z

Javaux EJ. Challenges in evidencing the earliest traces of life. *Nature* 2019;572(7770):451–460; doi: 10.1038/s41586-019-1436-4

Kminek G, Meyer MA, Beaty DW, et al. Mars Sample Return (MSR): Planning for Returned Sample Science. *Astrobiology* 2022;22(S1):S1–S4; doi: 10.1089/ast.2021.0198

Lemelle L, Simionovici AS, Schoonjans T, et al. Analytical requirements for quantitative X-ray fluorescence nanoimaging of metal traces in solid samples. *TrAC—Trends Anal Chem* 2017;91:104–111; doi: 10.1016/j.trac.2017.03.008

Lemelle L, Simionovici AS, Susini J, et al. X-ray imaging techniques and exobiology. *J Phys IV France* 2003;104(1): 377–380; doi: 10.1051/jp4:20030103

Lemelle L, Simionovici AS, Truche R, et al. A new nondestructive X-ray method for the determination of the 3D mineralogy at the micrometer scale. *Am Mineral* 2004;89(4): 547–553; doi: 10.2138/am-2004-0409

Lemelle L, Simionovici AS, Salomé M. et al. In situ search for life traces in extraterrestrial samples by synchrotron x-ray fluorescence 2D and 3D imaging. In: Proc. SPIE, Instruments, Methods, and Missions for Astrobiology X; 2007;6694: 669414; doi: 10.1117/12.733167

Lepot K. Signatures of early microbial life from the Archean (4 to 2.5 Ga) Eon. *Earth-Science Rev* 2020;209(July): 103296; doi: 10.1016/j.earscirev.2020.103296

Li Q, Chen X, Jiang Y, et al. Morphological identification of Actinobacteria. In: Actinobacteria—Basics and Biotechnological Applications IntechOpen; 2016; doi: 10.5772/61461

Little CTS, Johannessen KC, Bengtson S, et al. A late Paleoproterozoic (1.74 Ga) deep-sea, low-temperature, iron-oxidizing microbial hydrothermal vent community from Arizona, USA. *Geobiology* 2021;19(3):228–249; doi: 10.1111/gbi.12434

López-Archilla AI, Marin I, Amils R. Microbial community composition and ecology of an acidic aquatic environment: The Tinto River, Spain. *Microb Ecol* 2001;41(1):20–35; doi: 10.1007/S002480000044411 2001

Maldanis L, Hickman-Lewis K, Verezhak M, et al. Nanoscale 3D quantitative imaging of 1.88 Ga Gunflint microfossils reveals novel insights into taphonomic and biogenic characters. *Sci Rep* 2020;10(1):8163; doi: 10.1038/s41598-020-65176-w

McMahon S, Bosak T, Grotzinger JP, et al. A field guide to finding fossils on Mars. *J Geophys Res Planets* 2018;123(5):1012–1040 ; doi: 10.1029/2017JE005478

McMahon S, Jordan SF. A fundamental limit to the search for the oldest fossils. *Nat Ecol Evol* 2022;6(7):832–834; doi: 10 .1038/s41559-022-01777-0

Miot J, Benzerara K, Kappler A. Investigating microbe-mineral interactions: Recent advances in X-ray and electron microscopy and redox-sensitive methods. *Annu Rev Earth Planet Sci* 2014; 42(1):271–289; doi: 10.1146/annurev-earth-050212-124110

Nutman AP, Bennett VC, Friend CRL, et al. Rapid emergence of life shown by discovery of 3,700-million-year-old microbial structures. *Nature* 2016;537(7621):535–538; doi: 10.1038/nature19355

Odstrčil M, Odstrčil M, Holler M, et al. Alignment methods for nanotomography with deep subpixel accuracy. *Opt Express* 2019;27(25):36637–36652; doi: 10.1364/OE.27.036637

Parenteau MN, Cady SL. Microbial biosignatures in iron-mineralized phototrophic mats at Chocolate Pots hot springs, Yellowstone National Park, United States. *Palaios* 2010; 25(2):97–111; doi: 10.2110/palo.2008.p08-133r

Pfeiffer F. X-ray ptychography. *Nature Photon* 2018;12(1):9–17; doi: 10.1038/s41566-017-0072-5

Preston LJ, Shuster J, Fernández Remolar D, et al. The preservation and degradation of filamentous bacteria and biomolecules within iron oxide deposits at Rio Tinto, Spain. *Geobiology* 2011;9(3):233–249; doi: 10.1111/j.1472-4669.2011.00275.x

Ramijan K, Ultee E, Willemse J, et al. Stress-induced formation of cell wall-deficient cells in filamentous actinomycetes. *Nat Commun* 2018;9(1):5164; doi: 10.1038/s41467-018-07560-9

Rapin W, Ehlmann BL, Dromart G, et al. An interval of high salinity in ancient Gale crater lake on Mars. *Nat Geosci* 2019; 12(11):889–895; doi: 10.1038/s41561-019-0458-8

Sajjad W, Ilahi N, Kang S, et al. Endolithic microbes of rocks, their community, function and survival strategies. *Int Biodeterior Biodegrad* 2022;169(January):105387; doi: 10.1016/j .ibiod.2022.105387

Sánchez-Román M, Rivadeneyra MA, Vasconcelos C, et al. Biomineralization of carbonate and phosphate by moderately halophilic bacteria. *FEMS Microbiol Ecol* 2007;61(2):273–284; doi: 10.1111/j.1574-6941.2007.00336.x

Sauterey B, Charnay B, Affholder A, et al. Early Mars habitability and global cooling by H2-based methanogens. *Nat Astron* 2022;6(11):1263–1271; doi: 10.1038/s41550-022-01786-w

Schopf JW, Kudryavtsev AB, Sugitani K, et al. Precambrian microbe-like pseudofossils: A promising solution to the problem. *Precambrian Res* 2010;179(1–4):191–205; doi: 10 .1016/j.precamres.2010.03.003

Simon JI, Hickman-Lewis K, Cohen BA, et al. Samples collected from the floor of Jezero Crater with the Mars 2020 Perseverance rover. *JGR Planets* 2023;128(6); doi: 10.1029/ 2022je007474

Sumner DY. Poor preservation potential of organics in Meridiani Planum hematite-bearing sedimentary rocks. *J Geophys Res* 2004;109(E12):1–8; doi: 10.1029/2004JE002321

Tan J, Lewis JMT, Sephton MA. The fate of lipid biosignatures in a Mars-analogue sulfur stream. *Sci Rep* 2018;8(1):7586–7588; doi: 10.1038/s41598-018-25752-7

Thibault P, Dierolf M, Menzel A, et al. High-resolution scanning X-ray diffraction microscopy. *Science* 2008;321(5887): 379–382; doi: 10.1126/science.1158573

Thibault P, Guizar-Sicairos M. Maximum-likelihood refinement for coherent diffractive imaging. *New J Phys* 2012;14(6): 63004; doi: 10.1088/1367-2630/14/6/063004

Tolentino HC, Geraldes RR, Da Silva FM, *et al*. The CARNAÚBA X-ray nanospectroscopy beamline at the Sirius-LNLS synchrotron light source: Developments, commissioning, and first science at the TARUMÃ station. *J Electron Spectros Relat Phenomena* 2023;266:147340; doi: 10.1016/j.elspec.2023 .147340

Wakonig K, Stadler HC, Odstrcil M, et al. PtychoShelves, a versatile high-level framework for high-performance analysis of ptychographic data. *J Appl Crystallogr* 2020;53(Pt 2):574–586; doi: 10.1107/S1600576720001776

Zettler LAA, Gómez F, Zettler E, et al. Eukaryotic diversity in Spain's river of fire. *Nat* 2002;417(6885):137–137; doi: 10 .1038/417137a

Address correspondence to:
Lara Maldanis
ISTerre
Univ. Grenoble Alpes
Univ. Savoie Mont Blanc
CNRS, IRD, IFSTTAR
Grenoble
France

E-mail: laramcp@hotmail.com

Submitted November 15, 2023
Accepted June 18, 2024
Associate Editor: Sherry L. L. Cady

Abbreviations Used

DM = Difference map
EPFL = École Polytechnique Fédérale de Lausanne
EPMA = Electron probe microanalysis
FIB-SEM = Focused ion beam-scanning electron microscope
IUF = Institut Universitaire de France
ML = Maximum likelihood
PyXL = Ptychographic X-ray Computed Laminography
SEM = Scanning electron microscopy
tof-SIMS = Time-of-flight secondary ion mass spectrometry